# Designing Optimal Loop, Saddle, and Ellipse-Based Magnetic Coils by Spherical Harmonic Mapping

Peter J. Hobson, Noah L. Hardwicke, Alister Davis, Thomas X. Smith, Chris Morley, Michael Packer, Niall Holmes, Max A. Weil, Matthew J. Brookes, Richard Bowtell, and Mark Fromhold

***Abstract*— Adaptable, low-cost, coils designed by carefully selecting the arrangements and geometries of simple primitive units are used to generate magnetic fields for diverse applications. These extend from magnetic resonance and fundamental physics experiments to active shielding of quantum devices including magnetometers, interferometers, clocks, and computers. However, finding optimal arrangements and geometries of multiple primitive structures is time-intensive and it is challenging to account for additional constraints, for example, optical access, during the design process. Here, we demonstrate a general method to find these optimal arrangements. We encode specific symmetries into sets of loops, saddles, and cylindrical ellipses and then solve exactly for the magnetic field harmonics generated by each set. By combining these analytic solutions using computer algebra, we can use numerical techniques to efficiently map the landscape of parameters and geometries which the coils must satisfy. Sets of solutions may be found which generate desired target fields accurately while accounting for complexity and size restrictions. We demonstrate this approach by employing simple configurations of loops, saddles, and cylindrical ellipses to design target linear field gradients and compare their performance with designs obtained using conventional methods. A case study is presented where three optimized arrangements of loops, designed to generate a uniform axial field, a linear axial field gradient, and a quadratic axial field gradient, respectively, are hand-wound around a low-cost, 3-D-printed coil former. These coils are used to null the magnetic background in a typical laboratory environment, reducing the magnitude of the axial field along the central half of the former's axis from $(7.8 \pm 0.3)$ $\mu$T (mean $\pm$ standard deviation) to $(0.11 \pm 0.04)$ $\mu$T.**

***Index Terms*— Analytical models, coils, electromagnetic measurements, Fourier transforms, magnetic resonance, magnetic shielding, magnetometers, mathematical programming.**

## I. Introduction

EVERMORE sophisticated methods of magnetic field design are required to better null unwanted variations and generate targeted biases in precision measurement devices. Techniques to control magnetic fields have been applied for various precision measurements including in magnetic resonance scanners [1], [2], [3], electric dipole moment experiments [4], [5], [6], and Kibble balances for mass determination [7], [8], [9]. As well as this, precision magnetic field control is a necessity for new generations of quantum-enabled devices, including atomic magnetometers [10], [11], [12], [13], [14], [15], atom interferometers [16], [17], atom [18], [19] and ion [20] clocks, and quantum computers [21], [22]. Recently, the design of onboard coils for quantum-enabled devices has garnered extensive research interest [23], [24], [25], [26] as these coils must balance magnetic constraints, such as power efficiency and field uniformity, with significant nonmagnetic considerations, including optical access and ease of assembly.

Turner [27] pioneered the design of target coils from discretized surface currents, in which wires emulate a continuum of current flowing on a surface. Typically, the surface current is decomposed into a set of weighted orthogonal modes [28], [29], [30]. As these modes generate spatially orthogonal magnetic fields, the best combinations of weightings to generate a specified target field profile may be determined using simple mathematical programming [31], often least-squares minimization. However, the real-world performance of surface current-based coil systems is limited if the surface current is inaccurately emulated by the wire pattern. This is known as *discretization error* [32]. This error increases if the target field region is close to the coil or if manufacturing limitations prevent precise emulation of the surface current. In some cases, discretization error may be calculated analytically [33], [34], but often it may only be ascertained by numerically simulating each wire pattern a posteriori until a well-represented design is found. This may be very computationally intensive.

Unlike surface current-based coils, those directly designed from simple building blocks, including loops, saddles, and ellipses, hereby referred to as *primitives*, do not suffer from discretization error and have regular shapes, making them cheap and easy to manufacture. Roméo and Hoult [35] developed a method to design magnetic fields using these coils by exploiting the symmetries in a desired magnetic field, expressed using a spherical harmonic decomposition, with sets of primitives. They then maximized the target harmonic strength by tuning both the continuous geometric *coil parameters*, which determine the shape of the sets of primitives, and the discrete ratios of the number of turns of wire among different sets of primitives. Arrangements of multiple sets of primitives can produce a high-quality magnetic field since each

Manuscript received 9 February 2023; revised 8 May 2023; accepted 27 May 2023. Date of publication 16 June 2023; date of current version 23 June 2023. This work was supported in part by the U.K. Quantum Technology Hub Sensors and Timing under Grant EP/T001046/1, in part by the Innovate UK Project 44430 MAG-V: Enabling Volume Quantum Magnetometer Applications through Component Optimization and System Miniaturization, and in part by the Defence Science and Technology Laboratory. The Associate Editor coordinating the review process was Dr. Shisong Li. *(Peter J. Hobson and Noah L. Hardwicke contributed equally to this work.) (Corresponding author: Peter J. Hobson.)*

Peter J. Hobson, Noah L. Hardwicke, Alister Davis, Thomas X. Smith, Chris Morley, Michael Packer, Max A. Weil, and Mark Fromhold are with the School of Physics and Astronomy, University of Nottingham, NG7 2RD, United Kingdom (e-mail: peter.hobson@nottingham.ac.uk).

Niall Holmes, Matthew J. Brookes, and Richard Bowtell are with the School of Physics and Astronomy, University of Nottingham, NG7 2RD, United Kingdom and also with the Sir Peter Mansfield Imaging Centre, University of Nottingham, NG7 2RD, United Kingdom.

Digital Object Identifier 10.1109/TIM.2023.3284138

extra primitive provides additional parameters that one can optimize. However, the optimization of multiple primitives is challenging as each primitive generates many spherical harmonics. To design such systems, one may examine Taylor expansion coefficients [36], [37], [38], [39] of analytic expressions [23], [40], but these do not relate simply to the basis of spherical harmonics in many cases. This can make it difficult to ascertain how the minimization of different undesired variations should be prioritized to maximize field quality. Alternatively, numerically solved analytic formulations of the magnetic field [41], [42], [43] have been used effectively to design loops and saddles, but such approaches do not allow the relationship between the coil parameters and field quality to be determined a priori. As a result of these limitations, surface current-based coils are often preferred over primitive-based systems in settings where accurate target fields are required over large target regions relative to the coil size.

Here, we facilitate the wider use of primitive-based coil systems by providing a generalized approach to their design. We mathematically encode sets of primitive building blocks with spherical harmonic-like symmetries such that all magnetic field variations in free space generated by the sets may be encoded as exact, closed-form expressions. To achieve this, we impose the sets directly into Turner's surface current solution [27] and apply a spherical harmonic decomposition [35]. We solve the resulting integral equations analytically to determine the expansion coefficients as simple derivatives with respect to the coil parameters. Then, we use *Mathematica* to construct and simplify the analytic expressions for the expansion coefficients, upon which numerical root-finding routines search the coil parameter space for solutions that cancel field errors. By interpolating these solutions, we determine a meshed contour in the parameter space on which the solutions lie. We then rank the solutions according to a desired attribute, for example, field fidelity, power efficiency (field strength per unit current), inductance, or by practical concerns such as spatial extent, overlaps with access holes, or the distance between sets of primitives. We present three worked examples of this process—one of each using sets of loops, arcs, and ellipses primitives—to demonstrate the scope of our method, and compare each to standard equivalents. To finish, we design and build uniform axial, linear axial gradient, and quadratic axial gradient, field-generating loops on a 3-D-printed cylindrical coil former. We examine how this system can be used to null the background magnetic field in a typical laboratory environment.

The analytic model developed in this work was initially presented at the *Conference on Precision Electromagnetic Measurements 2022* [44].

## II. Mathematical Framework

### A. Field Harmonic Basis

In free space, the magnetic field can be represented as the gradient of a magnetic scalar potential, $\mathbf{B} = -\nabla\Psi$. The scalar potential and magnetic field both satisfy Laplace's equation, $\nabla^2\mathbf{B} = \nabla^2\Psi = 0$. Here, we express the magnetic scalar potential as the complete basis of real spherical harmonics and so the magnetic field may be expressed in terms of the complete basis of the vector derivatives of each real spherical harmonic [45]. We refer to this as the basis of *field harmonics*

$$\mathbf{B}(\mathbf{r}) = \sum_{n=1}^{\infty}\sum_{m=-n}^{n} f_{n,m}\mathbf{B}_{n,m}(\mathbf{r}) \tag{1}$$

where each field harmonic, with magnitude $f_{n,m}$, is denoted by $\mathbf{B}_{n,m}(\mathbf{r}) = \nabla h_{n,m}(\mathbf{r})$ and $h_{n,m}(\mathbf{r})$ is the spherical harmonic of the same order $n \in \mathbb{Z}^+$ and degree $m \in \mathbb{Z} \in [-n{:}n]$. Each spherical harmonic may be expressed as

$$h_{n,m}(r,\theta,\phi) = \eta_{n,m} r^n P_{n,|m|}(\cos\theta)\begin{pmatrix}\cos(m\phi)\\ \sin(|m|\phi)\end{pmatrix} \tag{2}$$

where the upper and lower terms in the right-hand-side bracket denote variations of degree $m \geq 0$ and $m < 0$, respectively. Each spherical harmonic has a zenith dependence described by Ferrer's associated Legendre polynomials, $P_{n,|m|}(\cos\theta)$. The harmonics are defined with the standard normalization

$$\eta_{n,m}\eta_{n',m'}\int_0^{\pi} d\theta \int_0^{2\pi} d\phi \times h_{n,m}(r_0,\theta,\phi)h_{n',m'}(r_0,\theta,\phi) = \delta_{n,n'}\delta_{m,m'} \tag{3}$$

on a unitary sphere, $r_0 = 1$, with

$$\eta_{n,m} = \sqrt{\frac{\zeta_{m,0}(2n+1)}{4\pi}\frac{(n-|m|)!}{(n+|m|)!}} \tag{4}$$

and $\zeta_{m,m'} = 2 - \delta_{m,m'}$, where $\delta_{m,m'}$ is the Kronecker delta function.

Here, we shall only consider $\cos(m\phi)$-like variations, for $m \geq 0$. Any $\sin(|m|\phi)$-like variations, for $m < 0$, may be generated by rotating the equivalent $\cos(m\phi)$-like variation by $\pi/(2|m|)$. The field harmonic components in Cartesian coordinates, $\mathbf{B}_{n,m}(\mathbf{r}) = X_{n,m}(\mathbf{r})\hat{\boldsymbol{x}} + Y_{n,m}(\mathbf{r})\hat{\boldsymbol{y}} + Z_{n,m}(\mathbf{r})\hat{\boldsymbol{z}}$, are presented in Appendix A. The axial component is

$$Z_{n,m}(r,\theta,\phi) = \eta_{n,m}(n+m)r^{n-1} \times P_{n-1,m}(\cos\theta)\cos(m\phi). \tag{5}$$

The symmetry of the axial component along the $z$-axis is determined by the parity of $(n+m-1)$ due to its dependence on $P_{n-1,m}(\cos\theta)$ [46]. Thus, the axial component is symmetric along the $z$-axis if $(n+m-1)$ is even and is antisymmetric along the $z$-axis if $(n+m-1)$ is odd.

The low-order field harmonics encode simple variations when expressed in Cartesian coordinates. For example, for $n = [1, 2]$ and $m = [0, 1]$, they are

$$\mathbf{B}_{1,0} = \frac{1}{2}\sqrt{\frac{3}{\pi}}\,\hat{\boldsymbol{z}} \tag{6}$$

$$\mathbf{B}_{1,1} = \frac{1}{2}\sqrt{\frac{3}{\pi}}\,\hat{\boldsymbol{x}} \tag{7}$$

$$\mathbf{B}_{2,0}(x,y,z) = \frac{1}{2}\sqrt{\frac{5}{\pi}}\left(-x\hat{\boldsymbol{x}} - y\hat{\boldsymbol{y}} + 2z\hat{\boldsymbol{z}}\right) \tag{8}$$

$$\mathbf{B}_{2,1}(x,z) = \frac{1}{2}\sqrt{\frac{15}{\pi}}\left(z\hat{\boldsymbol{x}} + x\hat{\boldsymbol{z}}\right) \tag{9}$$

as shown in Fig. 1.

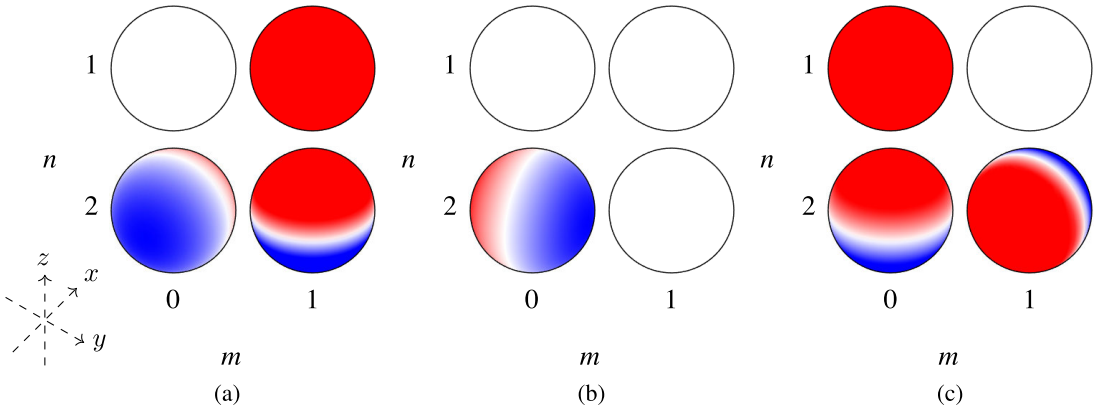


Fig. 1. Cartesian field harmonic components (a) $X_{n,m}(\mathbf{r})$, (b) $Y_{n,m}(\mathbf{r})$, and (c) $Z_{n,m}(\mathbf{r})$ (see (33)–(35), respectively, in Appendix A) of order $n \in [1, 2]$ and degree $m \in [0, 1]$ shown on the surface of unitary spheres (black outline; red-to-white-to-blue showing positive-to-zero-to-negative field harmonic amplitude), where $\mathbf{B}_{n,m}(\mathbf{r}) = X_{n,m}(\mathbf{r})\hat{\boldsymbol{x}} + Y_{n,m}(\mathbf{r})\hat{\boldsymbol{y}} + Z_{n,m}(\mathbf{r})\hat{\boldsymbol{z}}$, and $(\hat{\boldsymbol{x}}, \hat{\boldsymbol{y}}, \hat{\boldsymbol{z}})$ represent Cartesian unit vectors.

### B. Harmonic Matching

The magnetic field, (1), generated by the surface currents with $\cos(m\phi)$-like symmetry flowing on a cylinder of radius $\rho_c$ may be separated into contributions where the axial magnetic field has total symmetry (+) or total antisymmetry (−) along the $z$-axis about the origin

$$\mathbf{B}^{+}(\mathbf{r}) = \frac{\mu_0}{\pi} \sum_{\nu=0}^{\infty} \sum_{m=0}^{\infty} \frac{f_{2\nu+m+1,m}}{\rho_c^{2\nu+m+1}} \mathbf{B}_{2\nu+m+1,m}(\mathbf{r}) \tag{10}$$

$$\mathbf{B}^{-}(\mathbf{r}) = \frac{\mu_0}{\pi} \sum_{\nu=1}^{\infty} \sum_{m=0}^{\infty} \frac{f_{2\nu+m,m}}{\rho_c^{2\nu+m}} \mathbf{B}_{2\nu+m,m}(\mathbf{r}). \tag{11}$$

The axially symmetric field harmonics are of order $n = 2\nu + m + 1$ for $\nu \in \mathbb{Z}^{0+}$ and degree $m \in \mathbb{Z}^{0+}$. The axially antisymmetric field harmonics are of order $n = 2\nu + m$ for $\nu \in \mathbb{Z}^{+}$ and degree $m \in \mathbb{Z}^{0+}$.

As the magnetic field must relate uniquely to the scalar potential, the spatial forms of the field harmonics are preserved when examining the field generated by the surface current. Thus, the field harmonics must also be present within the well-known Green's function integral expression for the axial field in free space generated inside a cylindrical azimuthal surface current [27]. We express this in the axially symmetric and antisymmetric cases as

$$B_z^{+}(\rho, \phi, z) = -\frac{\mu_0}{\pi\rho_c} \sum_{m=0}^{\infty} \zeta_{m,0} \cos(m\phi) \times \int_0^{\infty} dk\ k \cos\left(\frac{kz}{\rho_c}\right) I_m\left(\frac{k\rho}{\rho_c}\right) K_m'(k) J_\phi^{m+}\left(\frac{k}{\rho_c}\right) \tag{12}$$

$$B_z^{-}(\rho, \phi, z) = -\frac{i\mu_0}{\pi\rho_c} \sum_{m=0}^{\infty} \zeta_{m,0} \cos(m\phi) \times \int_0^{\infty} dk\ k \sin\left(\frac{kz}{\rho_c}\right) I_m\left(\frac{k\rho}{\rho_c}\right) K_m'(k) J_\phi^{m-}\left(\frac{k}{\rho_c}\right) \tag{13}$$

where $I_m(z)$ and $K_m(z)$ represent the modified Bessel functions of the first and second kinds, respectively, of order $m$. The Fourier transforms of the axially symmetric and antisymmetric azimuthal current flows, $J_\phi^{+}(\mathbf{r}')$ and $J_\phi^{-}(\mathbf{r}')$, respectively, are

$$J_\phi^{m\pm}(k) = \frac{1}{2\pi} \int_0^{2\pi} d\phi'\ e^{-im\phi'} \int_{-\infty}^{\infty} dz'\ e^{-ikz'} J_\phi^{\pm}(\mathbf{r}'). \tag{14}$$

As detailed in Appendix B, we can transform the cylindrical variations in (12) and (13) into spherical variations like those in the axial field harmonic component, (5). We find

$$I_m\left(\frac{k\rho}{\rho_c}\right) \cos\left(\frac{kz}{\rho_c}\right) = \sum_{\nu=0}^{\infty} \frac{(-1)^\nu}{(2(\nu+m))!} \times \left(\frac{kr}{\rho_c}\right)^{2\nu+m} P_{2\nu+m,m}(\cos\theta) \tag{15}$$

$$I_m\left(\frac{k\rho}{\rho_c}\right) \sin\left(\frac{kz}{\rho_c}\right) = \sum_{\nu=1}^{\infty} \frac{(-1)^\nu}{(2(\nu+m)-1)!} \times \left(\frac{kr}{\rho_c}\right)^{2\nu+m-1} P_{2\nu+m-1,m}(\cos\theta). \tag{16}$$

Substituting (15) and (16) into (12) and (13) and grouping terms to match the field harmonic basis, (10) and (11), we find

$$f_{2\nu+m+1,m} = \frac{\zeta_{m,0}(-1)^{\nu+1}}{(2(\nu+m)+1)!} \left[\int_0^{\infty} dk\ k^{2\nu+m+1} K_m'(k) J_\phi^{m+}\left(\frac{k}{\rho_c}\right)\right] \tag{17}$$

$$f_{2\nu+m,m} = \frac{i\zeta_{m,0}(-1)^{\nu+1}}{(2(\nu+m))!} \left[\int_0^{\infty} dk\ k^{2\nu+m} K_m'(k) J_\phi^{m-}\left(\frac{k}{\rho_c}\right)\right]. \tag{18}$$

The axial field harmonic component is zero for harmonics of equal order and degree, $Z_{n,n}(\mathbf{r}) = 0$. To derive these magnitudes, we follow the same procedure as above using the transverse field, $B_x(\mathbf{r})$, from the well-known solution [27] and the transverse field harmonic component $X_{n,n}(\mathbf{r})$. The resulting integrals which determine the field harmonic magnitudes are the same as (17) and (18).

## III. Primitive Design

Now, we encode the azimuthal surface current on example sets of simple primitive building blocks: loops, saddles, and

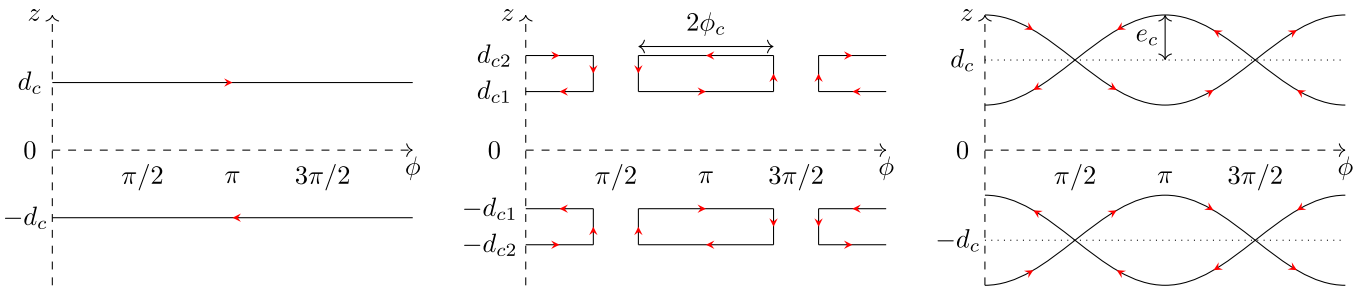


(a) (b) (c)

Fig. 2. Variation of primitive current patterns (red arrows indicate current flow direction) in the $\phi z$-plane on a cylinder of radius $\rho_c$ to generate the field harmonics optimized in the main text. (a) Axially antisymmetric loops separated axially by $2d_c$ generate field harmonics of order $N = 2\nu$, for $\nu \in \mathbb{Z}^+$, and degree $M = 0$. (b) Even number of pairs of axially symmetric sets of arcs with onefold symmetry along $\phi$, separated axially by $2d_{c1}$ and $2d_{c2}$ and which extend azimuthally by $2\phi_c$, may be connected to make saddles which generate field harmonics of order $N = 2\nu$ for $\nu \in \mathbb{Z}^+$ and degree $M = 2\mu + 1$ for $\mu \in \mathbb{Z}^+$. (c) Axially symmetric sets of ellipses with onefold symmetry along $\phi$, separated axially by $2d_c$ and which extend axially by a maximum of $e_c$, generate the same field harmonics as (b).

ellipses. We design the sets of primitives to have specific azimuthal and axial symmetries so that only certain field harmonics are present in the magnetic field. We then solve the field harmonic magnitude integrals, (17) and (18), analytically to exactly determine the magnitudes of the remaining field harmonics.

These solutions are used to choose the coil parameters of combinations of sets of primitives to generate target field harmonics. In Section III-A, we design axially antisymmetric loops to generate the $\mathbf{B}_{2,0}$ field harmonic and, in Section III-B, we design separate axially symmetric sets of saddles and ellipses to generate the $\mathbf{B}_{2,1}$ field harmonic. The optimization methodology we apply is presented in Section IV. The *Mathematica* programs we use to design each coil are publicly available for noncommercial use and are stored in the repository listed in [47]. The default arguments in each of the examples in the repository return the coil systems optimized in the main text.

### A. Linear Axial Gradient With Respect to Axial Position

The $\mathbf{B}_{2,0}$ field harmonic is contained within the axially antisymmetric field, (11), and has $m = 0$ azimuthal symmetry (no $\phi$-dependence). As such, it is generated by axially antisymmetric current flows with $m = 0$ azimuthal symmetry. These symmetries are matched by pairs of simple loops which carry equal and opposite current, $I$, and are separated about the origin by an axial distance $2d_c$ [see Fig. 2(a)]. We may represent such a pair of loops using the following azimuthal current density:

$$J_\phi^-(z') = I\big(\delta(z' - d_c) - \delta(z' + d_c)\big). \tag{19}$$

The Fourier transform, (14), of (19) is

$$J_\phi^{m-}(k) = -2iI\sin(kd_c)\delta_{m,0}. \tag{20}$$

We determine the field harmonic magnitudes by substituting (20) into (18)

$$f_{2\nu,0}(\chi_c) = \frac{2I}{(2\nu)!} \times \left[(-1)^\nu \int_0^\infty dk\ k^{2\nu}\sin(k\chi_c)K_1(k)\right] \tag{21}$$

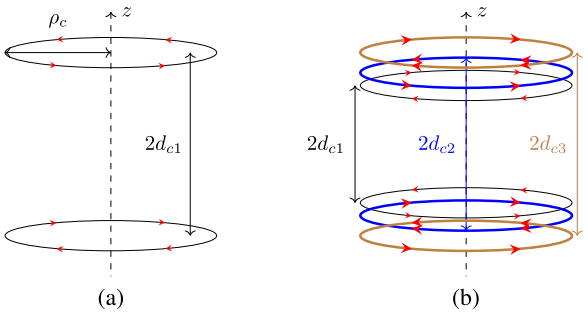


(a) (b)

Fig. 3. Schematics of $N_{\text{loops}}$ axially antisymmetric loop pairs (red arrows indicate current flow direction) of radius $\rho_c$ at axial positions $z' = \pm d_{ci}$ for $i \in [1{:}N_{\text{loops}}]$. (a) $N_{\text{loops}} = 1$ pair of loops with $d_{c1} = \big((3)^{1/2}/2\big)\rho_c$ (black). (b) $N_{\text{loops}} = 3$ pairs of loops with $d_{ci} = [0.5544, 0.6748, 0.8660]\rho_c$ and turn ratios 1:−2:2 (black, blue, and brown, respectively, with higher turn ratios in bold lines).

where the normalized separation is $\chi_c = d_c/\rho_c$. In Appendix C, we analytically solve the class of integrals, including (21), which encode the field harmonic magnitudes generated by loops. We find that

$$f_{2\nu,0}(\chi_c) = \frac{\pi I}{(2\nu)!}\frac{\partial^{2\nu}}{\partial\chi_c^{2\nu}}\left(\frac{\chi_c}{\sqrt{1+\chi_c^2}}\right). \tag{22}$$

We design $\mathbf{B}_{2,0}$ using (22) by choosing turn ratios and separations to maximize the $f_{2,0}$ field harmonic while minimizing all others. We then proceed by exactly nulling as many *leading-order* field harmonics as possible, which we define as the lowest order field harmonics generated by the selected primitive current pattern that are not the desired field harmonic. This is generally more effective than minimizing as many field harmonics as possible since the leading-order errors have the lowest spatial frequencies. In this specific case, as expected, the leading-order field harmonic, $f_{4,0}$, is nulled exactly for $\chi_c = (3)^{1/2}/2$ [see Fig. 3(a)]. This coil geometry may be referred to as an anti-Helmholtz pair/gradient-field Maxwell coil.

Here, we use *Mathematica* (as detailed in Section IV) to optimize three axially antisymmetric loop pairs, as presented in Fig. 3(b). We null $[f_{4,0}, f_{6,0}]$ and simultaneously maximize the

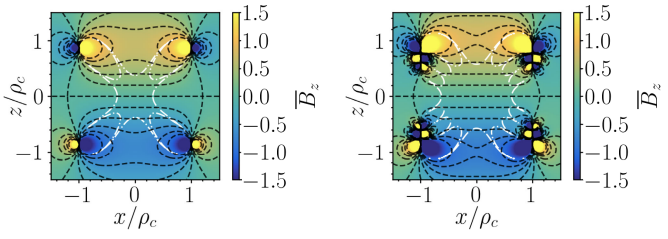


Fig. 4. Magnitude of the normalized axial magnetic field (color scales right), $\overline{B}_z = B_z/B_0$, where $B_0$ is the magnetic field gradient strength specified in Table I, in the $xz$-plane generated by the coils in Fig. 3(a) and (b), corresponding to (a) and (b), respectively, where the coils are of radius $\rho_c$. White contours enclose the regions where $\mathrm{d}B_z/dz$ deviates from perfect linearity by less than 1% (dot-dashed curves).

weighted sum of $f_{2,0}/f_{8,0}$, that is, the ratio of the target field harmonic magnitude to the magnitude of the next-leading-order error weighted by the respective turn ratios of each set of primitives. We also constrain all optimized separations to be less than or equal to that of an anti-Helmholtz pair, $\chi_c \leq (3)^{1/2}/2$, to make the generated design equally as applicable as an anti-Helmholtz pair in settings where the maximum axial extent of the system is limited, for example, due to experimental equipment.

In Fig. 4, the axial magnetic field generated by an anti-Helmholtz pair is compared to that generated by the optimized coil. The properties of the coils are summarized in Table I. The size of the central volume where $\mathbf{B}_{2,0}$ is generated with less than 1% error (less than 1% deviation from the target; bounded within the central dot-dashed curves in Fig. 4) is a factor of 2.85 greater than that generated by an anti-Helmholtz pair. However, due to the increased number of turns and alternating turn ratio polarities, compared to the anti-Helmholtz pair, the optimized coil is 1.17× times less power-efficient and has 5.24× greater inductance. In a scenario where fast current switching is required alongside high gradient linearity, the inductance could be calculated analytically [49] and imposed as an additional minimization condition.

### *B. Linear Transverse Gradient With Respect to Axial Position*

The $\mathbf{B}_{2,1}$ field harmonic is contained within the axially symmetric field, (10), and has $m = 1$ azimuthal symmetry (one line of symmetry in the $\rho\phi$ plane). To match this, we optimize sets of symmetric arcs of azimuthal extent $2\phi_c$, which are axially separated about the origin by $2d_c$ and have onefold azimuthal periodicity [the arc pairs repeat every $\phi = \pi$ with alternating polarity; Fig. 2(b)]. The azimuthal current density that describes one such set of arcs may be represented as

$$J_\phi^+(\phi', z') = I\big(\delta(z' - d_c) + \delta(z' + d_c)\big) \times \sum_{\lambda=0}^{1} (-1)^\lambda \big[H(\phi' + \phi_c - \lambda\pi) - H(\phi' - \phi_c - \lambda\pi)\big] \tag{23}$$

where $H(x)$ is the Heaviside step function. The Fourier transform, (14), of (23) is

$$J_\phi^{m+}(k) = \frac{2I\big(1 - (-1)^m\big)}{\pi m} \sin(m\phi_c)\cos(kd_c). \tag{24}$$

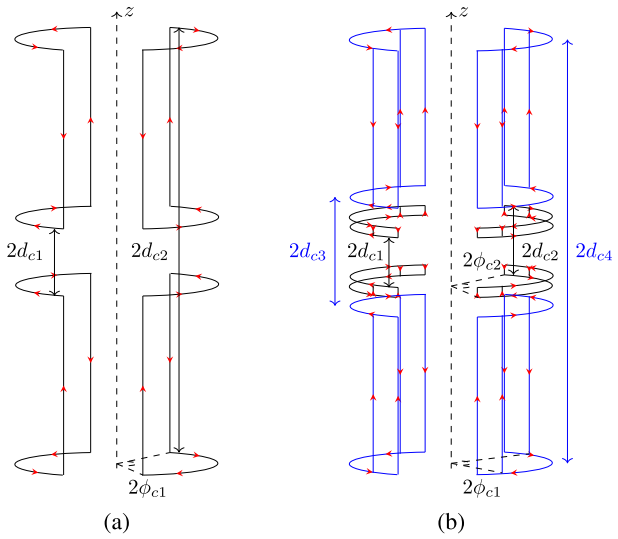


Fig. 5. Schematics of $N_{\text{arcs}}$ axially symmetric sets of arcs (red arrows indicate current flow direction) with onefold azimuthal symmetry of radius $\rho_c$ at axial positions $z' = \pm d_{ci}$ for $i \in [1{:}N_{\text{arcs}}]$ which are connected to make double saddles. (a) $N_{\text{arcs}} = 2$ sets of arcs (black) which extend azimuthally over $2\phi_{c1} = 2\pi/3$ and are at axial positions $d_{ci} = [0.404, 2.56]\rho_c$. The sets of arcs are connected in series to make double saddles. (b) $N_{\text{arcs}} = 4$ sets of arcs, each of which contains two nested azimuthal extensions, $2\phi_{c1} = 7\pi/15$ and $2\phi_{c2} = 13\pi/15$, at axial positions $d_{ci} = [0.2995, 0.4170, 0.6550, 2.5522]\rho_c$, where the first and second (black) and the third and fourth (blue) sets of arcs are connected in series to make double saddles with the same turn ratios.

Substituting (24) into (17), we find

$$f_{2\nu+m+1,m}(\chi_c, \phi_c) = \frac{4I\big(1 - (-1)^m\big)}{\pi m(2(\nu + m) + 1)!} \sin(m\phi_c) \times \left[(-1)^{\nu+1} \int_0^\infty dk\ k^{2\nu+m+1} \cos(k\chi_c) K_m'(k)\right]. \tag{25}$$

As with the case of the loop, we analytically solve the class of integrals, including (25), which encode the field harmonic magnitudes generated by arcs in Appendix C. We find

$$f_{2\nu+m+1,m}(\chi_c, \phi_c) = \frac{I(2m)!\big(1 - (-1)^m\big)}{2^{m-1}m!(2(\nu + m) + 1)!} \times \sin(m\phi_c) \frac{\partial^{2\nu+1}}{\partial \chi_c^{2\nu+1}} \left[\frac{\chi_c}{m}\left(\frac{1}{1+\chi_c^2}\right)^{m+1/2} + \sum_{k=0}^{m-1} \frac{(-1)^k}{2k+1}\binom{m-1}{k}\left(\frac{\chi_c^2}{1+\chi_c^2}\right)^{k+1/2}\right] \tag{26}$$

where the binomial coefficient is $\binom{n}{k} = n!/((n-k)!k!)$.

Now, we use (26) to select turn ratios, separations, and extents of four sets of arcs to maximize $f_{2,1}$ while minimizing leading-order errors. To obey current continuity, the number of sets of arcs must be even and the current in each set of arcs must correspond to an equal and opposite current in another set of arcs. As a result, we join each set of arcs to another to form double saddles [see Fig. 2(b)].

First, we note that (26) prohibits all even degrees and shows us that all field harmonics of odd degrees are proportional to $\sin(m\phi_c)$. We find optimal extents of multiple sets of arcs by substituting $\sin(m\phi_c)$ for the relevant Chebyshev polynomial [46] and then finding the root of the functions where

TABLE I

PROPERTIES OF THE STANDARD COILS IN FIGS. 3(a), 5(a), AND 7(a), DESIGNED USING THE METHODOLOGY PRESENTED IN ROMÉO AND HOULT [35], AND THE OPTIMIZED EQUIVALENTS IN FIGS. 3(b), 5(b), AND 7(b) DESIGNED IN THIS WORK FOR A COIL RADIUS OF $\rho_c = 10$ cm. THE FOLLOWING COIL PROPERTIES ARE LISTED: TARGET FIELD HARMONIC, $\mathbf{B}_{n,m}$ OF ORDER $n$ AND DEGREE $m$; THE MAXIMUM AXIAL DIMENSION, $\max(\dim_c)$, WHERE $\dim_c = d_c$ IN THE LOOPS AND SADDLES CASES, $\dim_c = d_c + e_c$ IN THE ELLIPSES CASE, $d_c$ IS THE SEPARATION OF THE COIL UNITS FROM THE ORIGIN, AND $e_c$ IS THE AXIAL EXTENT OF THE ELLIPSES FROM THEIR CENTER; THE TOTAL LENGTH OF THE WIRE IN THE COIL, $l$, INCLUDING REPEATED UNITS WITH MULTIPLE TURN RATIOS; THE MAGNETIC FIELD GRADIENT STRENGTH, $B_0$, THAT IS, $\mathrm{d}B_z/dz$ FOR $\mathbf{B}_{2,0}$ AND $\mathrm{d}B_x/dz$ FOR $\mathbf{B}_{2,1}$ ALONG THE $z$-AXIS AT THE CENTER OF THE COIL, PER UNIT CURRENT, $I$; THE INDUCTANCE, $L$; AND THE SIZE OF THE CENTRAL VOLUME WHERE THE TARGET FIELD GRADIENT IS GENERATED WITH LESS THAN 1% DEVIATION FROM TARGET RELATIVE TO THAT GENERATED BY THE STANDARD COIL, $V_{1\%}$. THE INDUCTANCE IS APPROXIMATED NUMERICALLY FROM THE TOTAL MAGNETIC ENERGY [48] USING COMSOL MULTIPHYSICS, ASSUMING THAT THE WIRE TRACKS ARE FILAMENTARY

| $\mathbf{B}_{n,m}$ | Coil | $\max(\dim_c)$, (cm) | $l$, (m) | $B_0/I$, ($\mu$T/Am) | $L$, ($\mu$H) | $V_{1\%}$ |
|---|---|---|---|---|---|---|
| $\mathbf{B}_{2,0}$ | Standard, Fig. 3a | 8.66 | 1.26 | 80.6 | 1.07 | 1 |
| | Optimized, Fig. 3b | 8.66 | 6.28 | 69.0 | 5.61 | 2.85 |
| $\mathbf{B}_{2,1}$ | Standard, Fig. 5a | 25.6 | 3.40 | 89.2 | 2.59 | 1 |
| | Optimized, Fig. 5b | 25.5 | 9.93 | 131 | 11.0 | 4.55 |
| | Standard, Fig. 7a | 22.5 | 3.06 | 95.0 | 2.85 | 1 |
| | Optimized, Fig. 7b | 11.5 | 5.18 | 16.8 | 1.40 | 6.26 |

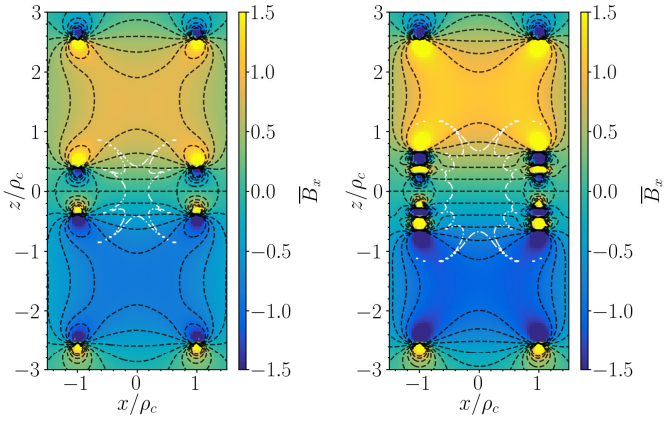


Fig. 6. Magnitude of the normalized transverse magnetic field (color scales right), $\overline{B}_x = B_x/B_0$, where $B_0$ is the magnetic field gradient strength specified in Table I, in the $xz$-plane generated by the coils in Fig. 5(a) and (b), corresponding to (a) and (b), respectively, where the coils are of radius $\rho_c$. White contours enclose the regions where $\mathrm{d}B_x/dz$ deviates from perfect linearity by less than 1% (dot-dashed curves).

leading-order degrees are nulled. Here, to null all field harmonics with $m = [3, 5]$, the required azimuthal extents of two sets of arcs with unitary turn ratios are $\phi_c = [7\pi/30, 13\pi/30]$. We then use *Mathematica* to optimize four sets of arcs (each of which has two nested azimuthal extensions) to null the leading-order errors, $[f_{4,1}, f_{6,1}, f_{8,1}]$, and maximize the weighted sum of $f_{2,1}/f_{10,1}$ generated by the four sets of arcs. As with Section III-A, we also constrain all axial separations, here to $\chi_c \leq 2.56$, so that the maximum extent is less than or equal to that of a standard design created in [35] [see Fig. 5(a)].

The optimized coil design is presented in Fig. 5(b). In Fig. 6, we show that the optimized coil generates $\mathbf{B}_{2,1}$ much more effectively than the standard coil. The power efficiency of the optimized coil is 1.47× greater and it generates $\mathbf{B}_{2,1}$ with less than 1% error over a central region that is 4.55× greater in volume (see Table I). Compared with the standard coil, however, as with Section III-A, the increased complexity of the optimized coil arrangement increases the comparative inductance by a factor of 4.25.

Given the acute changes in flow direction in saddles between current-carrying arcs and axial connecting wires, inaccuracy in saddle construction may generate unwanted high-order field harmonics [35]. To overcome this, we can use smoothly varying elliptical wire tracks on the surface of a cylinder instead of saddles to generate the same field harmonics.

Here, we demonstrate this by generating $\mathbf{B}_{2,1}$ using sets of axially symmetric cylindrical ellipses, which each extend over an axial distance $2e_c$ and are separated about the origin by a central axial distance $2d_c > 2e_c$. The sets of ellipses do not cross, preserving the axial symmetry, and have onefold azimuthal periodicity [the ellipse pairs repeat every $\phi = \pi$ with alternating polarity; Fig. 2(c)]. The azimuthal current density which traces the path of one such set of ellipses may be represented as

$$J_\phi^+(\phi', z') = I \sum_{\lambda=0}^{1} (-1)^\lambda \big[\delta\big(z' - \big(d_c + e_c \cos\big(\phi' - \lambda\pi\big)\big)\big) + \delta\big(z' + \big(d_c + e_c \cos\big(\phi' - \lambda\pi\big)\big)\big)\big]. \tag{27}$$

The Fourier transform, (14), of (27) is

$$J_\phi^{m+}(k) = -2Ii^{m+1}\big(1 - (-1)^m\big) J_m(ke_c) \sin(kd_c) \tag{28}$$

where $J_m(z)$ represents the Bessel function of the first kind of order $m$. Substituting (28) into (17), we find

$$f_{2\nu+m+1,m}(\chi_c, \psi_c) = \frac{4I\big(1 - (-1)^m\big)}{(2(\nu + m) + 1)!} \times \left[(-1)^{\nu+(m+3)/2} \times \int_0^\infty dk\ k^{2\nu+m+1} J_m(k\psi_c) \sin(k\chi_c) K_m'(k)\right] \tag{29}$$

where the normalized extent is $\psi_c = e_c/\rho_c$.

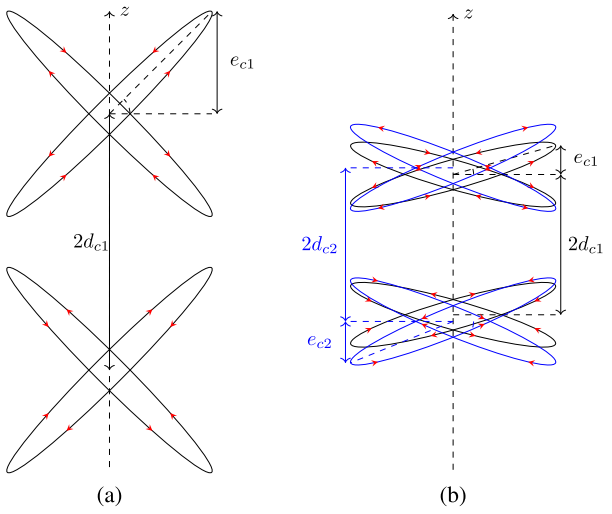


Fig. 7. Schematics of $N_{\text{ellipses}}$ axially symmetric sets of ellipses (red arrows indicate current flow direction) with onefold azimuthal symmetry of radius $\rho_c$ at axial positions $z' = \pm d_{ci}$ for $i \in [1{:}N_{\text{ellipses}}]$. (a) $N_{\text{ellipses}} = 1$ set of ellipses with $d_{c1} = 1.25\rho_c$ and which extend by a maximum axial distance $e_{c1} = \rho_c$ (black). (b) $N_{\text{ellipses}} = 2$ sets of ellipses with $d_{ci} = [0.6842, 0.7493]\rho_c$ which extend by maximum axial distances $e_{ci} = [0.2842, 0.4036]\rho_c$ and have opposite current ratios, 1:−1 (black and blue, respectively).

We solve the class of integrals that include (29) analytically in Appendix D. We find

$$f_{2\nu+m+1,m}(\chi_c, \psi_c) = \frac{8I}{(2(\nu+m)+1)!}(-1)^{m+1} \times \frac{\partial^{2\nu+1}}{\partial \chi_c^{2\nu+1}} \left[\chi_c \frac{\partial^m \tilde{S}_m(\chi_c,\psi_c)}{\partial \chi_c^m} + m \frac{\partial^{m-1} \tilde{S}_m(\chi_c,\psi_c)}{\partial \chi_c^{m-1}} + \psi_c \frac{\partial^m \tilde{S}_m(\chi_c,\psi_c)}{\partial \chi_c^{m-1} \partial \psi_c}\right] \tag{30}$$

where

$$\tilde{S}_m(\chi_c, \psi_c) = \frac{(1-i)}{2i^m\sqrt{2\psi_c}} Q_{m-1/2}\left(i\frac{\psi_c^2 - \chi_c^2 - 1}{2\psi_c}\right) \tag{31}$$

and $Q_{m-1/2}(z)$ represents a Legendre function of the second kind of half-integer order, $(m - 1/2)$.

Now, we use (30) to select turn ratios, separations, and extents of two sets of ellipses to maximize $f_{2,1}$ while minimizing leading-order errors. Unlike the case of the saddle, the optimization of orders and degrees cannot be separated. Thus, to maximize a field harmonic using two sets of ellipses, we completely null the leading-order magnitudes, $[f_{4,1}, f_{4,3}, f_{6,1}]$, and maximize the weighted ratio of $f_{2,1}/f_{8,1}$ generated by both sets of ellipses. Additionally, we impose $(\chi_c + \psi_c) \leq 1.32$ to limit the maximum system dimension to be less than or equal to half that of the optimized saddle coils.

In Figs. 7 and 8, we present schematics and performances of a standard coil design from [35] and the optimized design, respectively. As expected, the optimized elliptical coils are effective at generating $\mathbf{B}_{2,1}$ even with the constraint on system extent. Compared to the standard double saddles [see Fig. 5(a)] and ellipses [see Fig. 7(a)], the optimized elliptical coil has a maximum axial extent 2.22× and 1.96× smaller, but generates $\mathbf{B}_{2,1}$ with less than 1% error over central volumes 1.36× and 6.26× greater in size. However, due to opposite directions

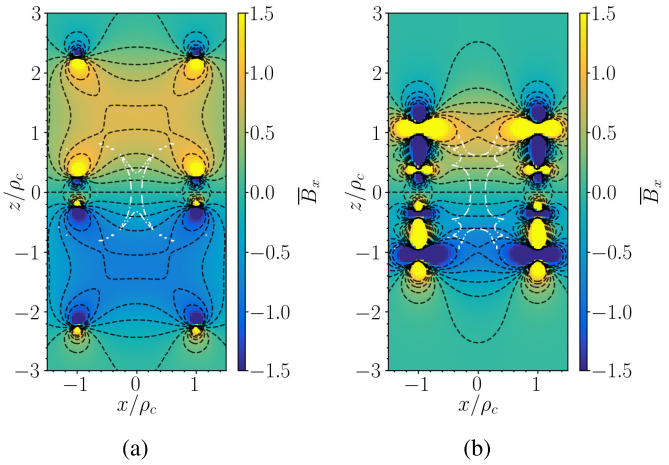


Fig. 8. Magnitude of the normalized transverse magnetic field (color scales right), $\overline{B}_x = B_x/B_0$, where $B_0$ is the magnetic field gradient strength specified in Table I, in the $xz$-plane generated by the coils in Fig. 7(a) and (b), corresponding to (a) and (b), respectively, where the coils are of radius $\rho_c$. White contours enclose the regions where $\mathrm{d}B_x/dz$ deviates from perfect linearity by less than 1% (dot-dashed curves).

of current polarity between the two sets of ellipses in the optimized design, the standard coils are 5.31× and 5.65× more power-efficient than the optimized elliptical coil.

## IV. Optimization Routine

Our goal is to find an *optimal* set of coil parameters that maximize a desired field harmonic while minimizing unwanted contributions. We shall only consider optimization of continuous geometric parameters, not discrete turn ratios which we specify alongside other properties like the minimum separation between primitives. To determine the best turn ratios, we rerun the optimization for simple combinations of turn ratios and then rank solutions across all runs.

Each coil parameter affords a degree of freedom with which to null a field harmonic. In theory, it is possible to null as many field harmonics as there are coil parameters, but in nontrivial scenarios, these solutions are difficult to find and may not exist within the constrained parameter space. Instead, we consider an underdetermined problem system, that is, we null fewer field harmonics than there are coil parameters. In the space of coil parameters, the solutions lie on a contour of dimension equal to the number of coil parameters less the number of nulled harmonics. Finding a solution on this contour using numerical techniques is faster and more reliable than finding a single-point solution. Increasing the dimensionality of the contour makes it easier to find solutions at the expense of nulling fewer harmonics. Once solutions are found on a contour, we rank them according to a desired property, such as the ratio of the desired-to-leading-order-error harmonic magnitudes, and then select the best-ranked solution. We implement the optimization in *Mathematica* because of its fast and easy-to-use symbolic expression simplification (via the `Simplify` function), numerical root-finding (via the `FindRoot` function), and process parallelization.

Let us consider the design presented in Section III-A to generate $\mathbf{B}_{2,0}$ using $N_{\text{loops}} = 3$ pairs of loops. Our optimization algorithm is summarized in Fig. 9.

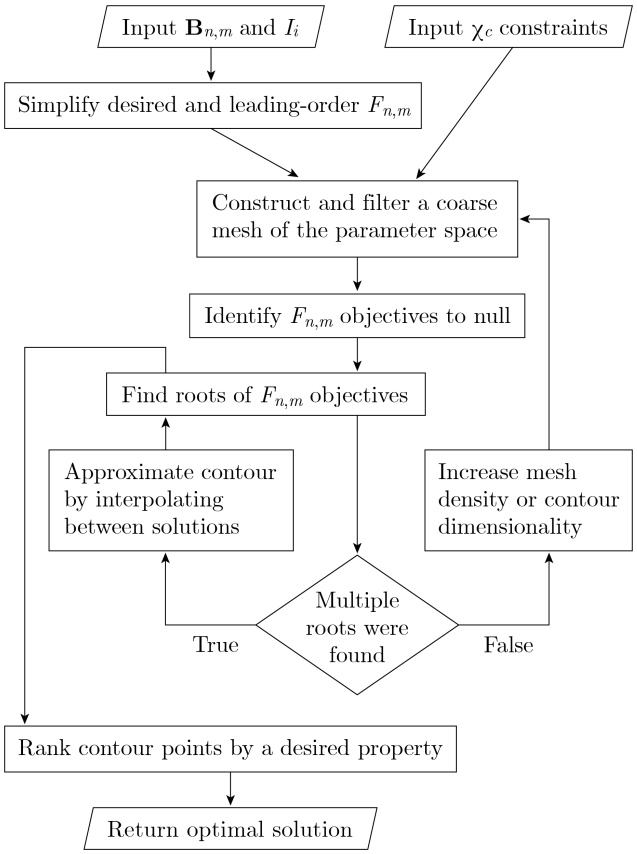


Fig. 9. Algorithm used to determine optimal sets of normalized coil separations, $\chi_c$. The inputs are: a target field harmonic, $\mathbf{B}_{n,m}$, of order $n$ and degree $m$; turn ratios of primitive groups, $I_i$; and constraints on the values of $\chi_c$. The weighted magnitudes of field harmonics, $F_{n,m}$, are used to search the parameter space for solutions on the contours where the set of leading-order harmonics are nulled. These solutions are ranked and the optimal solution is returned.

First, we construct and simplify symbolic expressions for the total magnitudes of the low-order field harmonics generated by the primitive set, weighted by the predetermined turn ratios. The weighted magnitude of each field harmonic is

$$F_{n,0} = \sum_{i=1}^{N_{\text{loops}}} I_i f_{n,0}(\chi_{ci}) \tag{32}$$

where $I_i$ are the turn ratios of each loops pair and the individual field harmonic magnitudes, $f_{n,0}$, may be obtained using (22). We use (32) as the objective function to search for solutions of $F_{4,0} = F_{6,0} = 0$ in a coarse mesh of the $N_{\text{loops}}$-dimensional parameter space. In this design, three filtering conditions are applied to the mesh to bound the search space and impose a minimum distance between adjacent coil pairs: $\chi_{ci} \geq 0.1$, $\chi_{ci} \leq (3)^{1/2}/2$, and $(\chi_{c(i+1)} - \chi_{ci}) \geq 0.01$. This reduces the number of mesh points to 1140 [see Fig. 10(a)].

At each mesh point, we apply `FindRoot`, which uses a Newton–Raphson method with step control [50] to search locally around positions in the solution space for locations where the undesired harmonics are nulled. The search over

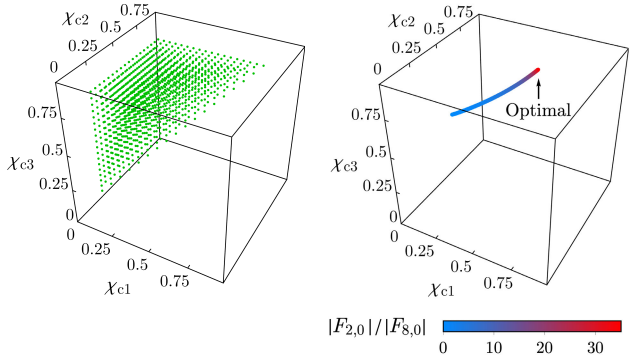


Fig. 10. (a) Initial seeds (green scatter) for the `FindRoot` function in *Mathematica* in the search space of optimal normalized separations, $\chi_{ci}$, for $i \in [1{:}N_{\text{loops}}]$, to design the set of $N_{\text{loops}} = 3$ axially antisymmetric loop pairs presented Fig. 3(b). (b) Contour of solutions in the search space of $\chi_{ci}$ that null the field harmonics of undesired orders $n = [4, 6]$ and degree $m = 0$. Coloring corresponds to the magnitude of the ratio of the weighted sum of the magnitudes of the target field harmonic generated by the set of loop pairs, $F_{2,0}$, to that of the leading-order error field harmonic generated by the set of loop pairs, $F_{8,0}$. The optimal solution (arrow) maximizes this ratio.

1140 points takes 0.65 s to complete[1] and 21 unique points are found on the 1-D solution contour. We then linearly interpolate between the known points on the solution contour to estimate further solutions. The interpolated points are randomized slightly to expand the evaluation scope and are then used to seed `FindRoot` once more. This process occurs at 411 interpolated points and takes 0.18 s. This is more efficient than the previous step because the seeds are close to the solution contour and therefore converge rapidly. In this example, all the interpolated seeds converge onto the solution contour, which is shown in Fig. 10(b), but in cases where the contour is discontinuous or varies greatly, not all seeds may converge. Finally, we rank the solutions on the contour according to the absolute value of the ratio of the magnitude of the desired field harmonic, $F_{2,0}$, to the leading-order error field harmonic, $F_{8,0}$. We select the solution that maximizes this ratio [denoted with an arrow in Fig. 10(b)], which takes 0.01 s for the $\mathbf{B}_{2,0}$ example.

## V. Case Study: Axial Nulling

Now, we present a case study demonstrating the implementation of optimized magnetic field coils to null residual axial variations in free space, for example, for residual field compensation for atomic magnetometers [13] or atom interferometers [17].

The system comprises the loop coil in Fig. 3(b) which generates the $\mathbf{B}_{2,0}$ field harmonic, along with other loop coils (presented in Appendix E) designed using our open-access *Mathematica* program to generate the $\mathbf{B}_{1,0}$ and $\mathbf{B}_{3,0}$ field harmonics. We choose to generate these field harmonics as they are the lowest order $m = 0$ field harmonics [35], and so are most likely to be present in the background field. The coils are

[1]Calculations are bench-marked using a *MacBookPro18,2* equipped with an *M1 Max* processor with eight 3228-MHz *performance* cores, two 2064-MHz *efficiency* cores, and 32 GB of 512-bit LPDDR5 SDRAM memory.

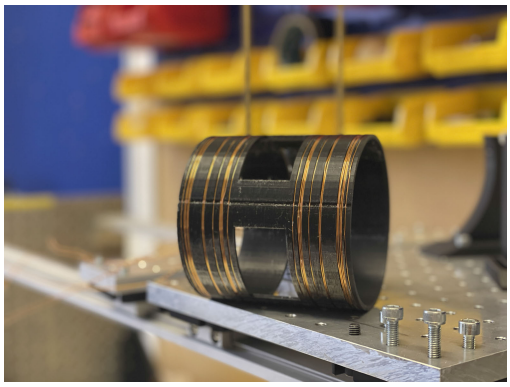

Fig. 11. Hand-wound 3-D-printed coil former containing independent uniform axial, $B_z$, linear axial gradient, $\mathrm{d}B_z/dz$, and quadratic axial gradient, $\mathrm{d}^2B_z/dz^2$, field-generating coils.

wound by hand using 0.63 mm diameter (22 AWG) enameled copper wire on a coil former of a radius of $\rho_c = 50$ mm (see Fig. 11). During optimization, the normalized axial separations are bounded between $0.35 < \chi_c < 1$. This allows the coil former to be only 100 mm long and leaves a large central axial region of length 35 mm where there are no wires. This area contains four optical access holes that are evenly spaced and have a height of 30 mm and an azimuthal extent of $\pi/3$ radians. The coil former is manufactured using fused deposition modeling (FDM) with a commercially available UltiMaker S5 using hard PLA body material and PVA support material. The PVA support is dissolved during postprocessing by soaking the print in lukewarm water for 48 h. The FDM printer is capable of rendering grooves in the coil former with a resolution of 0.06 mm and uses cost-effective materials (< £20 in this scenario).

The axial magnetic field generated by each coil is measured using a Stefan Mayer Fluxmaster magnetometer connected to an NI-USB 6212 data acquisition system. During each measurement, sinusoidal currents of amplitude 80 mA and oscillating at a frequency of 5 Hz are passed through each coil in turn for 7 s. The magnetic field produced by each coil is obtained by calculating the fast Fourier transform (FFT) of the magnetometer output, eliminating the need for separate measurement offsets. The measured and expected field profiles show excellent agreement and are presented in Fig. 12(a).

Next, the static axial magnetic field along the central 50 mm of the coil's axis is decomposed into uniform, linear gradient, and quadratic gradient contributions using the method of least-squares, following the method in [51]. Coil currents of $I = ([178, 59, 9]\pm 1)$ mA are applied to the $\mathbf{B}_{1,0}$, $\mathbf{B}_{2,0}$, and $\mathbf{B}_{3,0}$ field-generating coils, respectively, to null the measured static background. The magnitude of the axial field pre- and postnull is shown in Fig. 12(b). Over the central 50 mm of the coil's axis, the mean axial field magnitude reduces by over a factor of 70 from 7.8 to 0.11 $\mu$T and the standard deviation in the axial field magnitude reduces by over a factor of 7 from 300 to 40 nT. To further diminish the axial field, several approaches could be considered, such as adding more field-generating coils to null higher-order field harmonics, increasing the number of leading orders nulled in existing coil designs by increasing the number of separations optimized, or incorporating dynamic feedback from a reference magnetometer to update the applied coil currents [52].

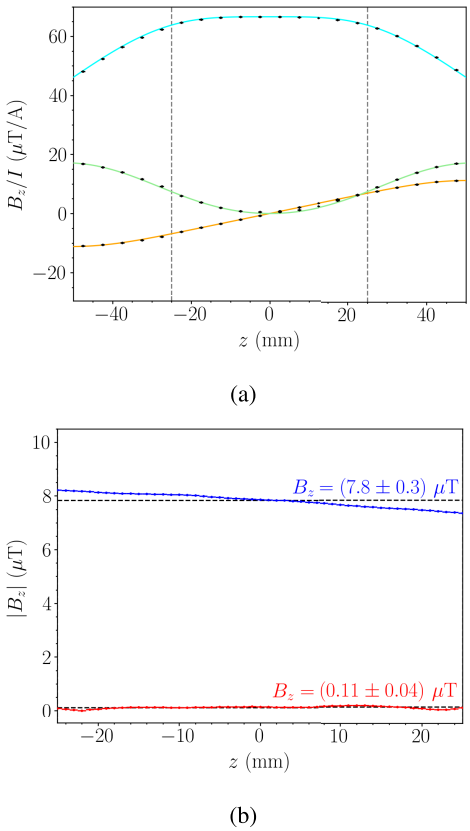


Fig. 12. (a) Magnitude of the axial magnetic field, $B_z$, per unit current, $I$, along the $z$-axis, generated by the uniform (light blue curve), linear gradient (orange curve), and quadratic gradient (light green curve) axial field-generating coils presented in Figs. 13(a), 3(b), and 13(b), alongside experimental measurements (black scatter). The magnetic null region is shown with dashed lines (gray). (b) Measured static axial magnetic field magnitude without active nulling (blue curve) and with active nulling (red curve), alongside labels (blue and red) displaying the mean (also shown with black dashed curves) and standard deviation in the axial field magnitude within the null region.

## VI. Conclusion and Outlook

Here, we have presented a spherical harmonic decomposition of the magnetic field in free space generated inside sets of primitive structures based on loops, saddles, and ellipses. In each case, we solved for the magnetic field harmonic magnitudes as simple derivatives with respect to the coil parameters. These derivatives can be computed rapidly using computer algebra software, and in this work we used *Mathematica*. We then demonstrated a generalized approach to design simple primitive coil structures by mapping the landscape of parameters that control the geometry of each set. Using this approach, we designed three field-generating structures—nested sets of loops, arcs, and ellipses—which generate target fields accurately by completely nulling a set number of leading-order undesired contributions. To allow a fair comparison with standard systems, in each worked example, we chose the solutions closest to the global optimum (which null the leading-order deviations while maximizing the

target-field-to-next-leading-order-error ratio) within the constrained space of coil parameters. However, the optimization procedure could be readily adjusted to prioritize other constraints such as power efficiency, size, and inductance. Furthermore, more diverse objective functions could also be added to ensure that designs can be manufactured easily, for example, sensitivity to wire misplacement or the number of wire overlaps.

Although we have focused on specific worked examples within the main text, the *Mathematica* program we provide [47] may be used to design any low-order field harmonic using the integral solutions in Appendices C and D. We use the loops coil optimized in the main text, alongside other loops coils generated using our program (see Appendix E), to construct a 3-D-printed, hand-wound axial field compensation system. By calculating the appropriate currents applied to the coil, we were able to significantly reduce both the magnitude and variation in the measured axial field along the central half of the coil's axis in a typical laboratory environment. Specifically, we were able to reduce the axial field magnitude from 7.8 $\mu$T to 0.11 $\mu$T and its standard deviation from 300 to 40 nT.

One can design any magnetic field in free space using our program by decomposing the target field into a weighted sum of field harmonics and combining sets of axially symmetric and antisymmetric primitives. Optimized arrangements of primitive coils may be useful in diverse contexts such as the design of accurate and power-efficient linear gradient fields for magneto-optical traps [53] or the cancellation of external interference for atomic magnetometers [51] by using modified governing equations accounting for the response of external passive magnetic shielding [32]. The field harmonics generated by primitives could also be posed and solved for other surface geometries. For example, cuboidal primitives may be useful for generating magnetically shielded enclosures [54] and toroidal primitives may be applied for plasma confinement in tokamaks [55]. Discrete building blocks and discretized surface current-based coils could also be implemented together to maximize their performance, for example, broadband reduction in the noise floor using power-efficient simple building block coils combined with accurate shimming of residual field harmonics using complex surface current-based coil patterns. Alternatively, one may modify and resolve the governing equations to impose more complex primitives, such as combinations of axially symmetric and antisymmetric units with predetermined turn ratios. This may be useful for applications where a single coil is required to generate a target magnetic field profile composed of multiple field harmonics with different symmetries.

Our optimization approach may also be applied in other settings where there are diverse contributions that need to be minimized and maximized simultaneously, including aerofoil design [56] and perturbation analysis in optimization problems [57].

## Appendix A
## Field Harmonic Components

Following Roméo and Hoult [35], we calculate the vector gradient of the spherical harmonics of degree $m \geq 0$, (2), to find the field harmonics, $\mathbf{B}_{n,m}(\mathbf{r}) = X_{n,m}(\mathbf{r})\hat{\boldsymbol{x}} + Y_{n,m}(\mathbf{r})\hat{\boldsymbol{y}} + Z_{n,m}(\mathbf{r})\hat{\boldsymbol{z}}$, where

$$\begin{aligned} &X_{n,m}(r,\theta,\phi) \\ &= \eta_{n,m} r^{n-1}\Bigg[-\frac{1+\delta_{m,0}}{2} \times P_{n-1,m+1}(\cos\theta)\cos((m+1)\phi) \\ &\qquad + \frac{(1-\delta_{m,0})(n+m-1)(n+m)}{2} \\ &\qquad \times P_{n-1,m-1}(\cos\theta)\cos((m-1)\phi)\Bigg] \end{aligned} \tag{33}$$

$$\begin{aligned} &Y_{n,m}(r,\theta,\phi) \\ &= \eta_{n,m} r^{n-1}\Bigg[-\frac{1+\delta_{m,0}}{2} \times P_{n-1,m+1}(\cos\theta)\sin((m+1)\phi) \\ &\qquad - \frac{(1-\delta_{m,0})(n+m-1)(n+m)}{2} \\ &\qquad \times P_{n-1,m-1}(\cos\theta)\sin((m-1)\phi)\Bigg] \end{aligned} \tag{34}$$

$$\begin{aligned} &Z_{n,m}(r,\theta,\phi) \\ &= \eta_{n,m}(n+m) r^{n-1} \times P_{n-1,m}(\cos\theta)\cos(m\phi). \end{aligned} \tag{35}$$

## Appendix B
## Matching Cylindrical and Spherical Field Variations

First, let us consider the standard series expansions [46]

$$I_m(x) = \sum_{l=0}^{\infty} \frac{1}{l!(l+m)!}\left(\frac{x}{2}\right)^{2l+m} \tag{36}$$

$$\cos(y) = \sum_{l=0}^{\infty} \frac{(-1)^l y^{2l}}{(2l)!}. \tag{37}$$

To match the variations in (36) and (37) with the arguments of (12), $x = k\rho/\rho_c$ and $y = kz/\rho_c$, we group the terms with common exponents of $k$ and then convert to spherical coordinates, $\rho = r\sin\theta$ and $z = r\cos\theta$. We find

$$\begin{aligned} I_m\left(\frac{k\rho}{\rho_c}\right)\cos\left(\frac{kz}{\rho_c}\right) &= \left(\frac{kr\sin\theta}{2\rho_c}\right)^m \sum_{\nu=0}^{\infty}\sum_{l=0}^{\nu} \frac{1}{(\nu-l)!(\nu-l+m)!} \\ &\quad \times \frac{(-1)^l}{2^{2(\nu-l)}(2l)!}\left(\frac{kr}{\rho_c}\right)^{2\nu} \cos^{2l}\theta \sin^{2(\nu-l)}\theta. \end{aligned} \tag{38}$$

We now introduce the expansion of the associated Legendre polynomials, as derived in [58]

$$P_{n,m}(x) = 2^n\left(1-x^2\right)^{m/2} \times \sum_{l=m}^{n} \frac{l!}{(l-m)!} x^{l-m}\binom{n}{l}\binom{\frac{n+l-1}{2}}{n}. \tag{39}$$

We substitute $x = \cos\theta$ into (39) and reindex to $n = 2\nu + m$ and $l = l' + m$, finding

$$\begin{aligned} &P_{2\nu+m,m}(\cos\theta) \\ &= 2^{2\nu+m}\sin^m\theta \\ &\quad \times \sum_{l'=0}^{2\nu} \frac{(l'+m)!}{l'!}\binom{2\nu+m}{l'+m}\binom{\nu+m+\frac{l'-1}{2}}{2\nu+m}\cos^{l'}\theta. \end{aligned} \tag{40}$$

For a fixed value of $\nu$, one may factorize out the variations proportional to $\sin^m\theta$ in (38) and (40) by examining the $l = l' = 0$ terms. We can, therefore, match these variations together, with an unknown scaling, and invert to find the scaling. We find

$$I_m\left(\frac{k\rho}{\rho_c}\right)\cos\left(\frac{kz}{\rho_c}\right) = \sum_{\nu=0}^{\infty}\frac{(-1)^\nu}{(2(\nu+m))!}\times\left(\frac{kr}{\rho_c}\right)^{2\nu+m} P_{2\nu+m,m}(\cos\theta). \quad (41)$$

Similarly, following the same method using the standard series expansion of $\sin(y)$ [46] and reindexing (39) to $n = 2\nu + m - 1$, we find

$$I_m\left(\frac{k\rho}{\rho_c}\right)\sin\left(\frac{kz}{\rho_c}\right) = \sum_{\nu=1}^{\infty}\frac{(-1)^\nu}{(2(\nu+m)-1)!}\times\left(\frac{kr}{\rho_c}\right)^{2\nu+m-1} P_{2\nu+m-1,m}(\cos\theta). \quad (42)$$

## Appendix C
## Solving the Loops and Saddles Harmonic Weighting Function

Here, we obtain the complete class of integrals

$$\beta^+_{2\nu+m+1,m}(\chi_c) = (-1)^{\nu+1}\int_0^\infty dk\ k^{2\nu+m+1}\cos(k\chi_c)K'_m(k) \quad (43)$$

$$\beta^-_{2\nu+m,m}(\chi_c) = (-1)^{\nu+1}\int_0^\infty dk\ k^{2\nu+m}\sin(k\chi_c)K'_m(k) \quad (44)$$

which we shall refer to as the symmetric and antisymmetric cases, respectively, for $\nu \in \mathbb{Z}^{0+}$ and $m \in \mathbb{Z}^{0+}$. We shall use the standard result [59]

$$\int_0^\infty dk\ k^m\cos(k\chi_c)K_m(k) = \frac{\pi(2m)!}{2^{m+1}m!}\left(\frac{1}{1+\chi_c^2}\right)^{m+1/2}. \quad (45)$$

First, we integrate the left-hand side of (45) by parts

$$\int_0^\infty dk\ k^m\cos(k\chi_c)K_m(k) = -\frac{1}{\chi_c}\int_0^\infty dk\ k^m\sin(k\chi_c)K'_m(k) - \frac{m}{\chi_c}\int_0^\infty dk\ k^{m-1}\sin(k\chi_c)K_m(k) \quad (46)$$

which we can rearrange to show

$$\int_0^\infty dk\ k^m\sin(k\chi_c)K'_m(k) = -\chi_c\int_0^\infty dk\ k^m\cos(k\chi_c)K_m(k) - m\int_0^\infty dk\ k^{m-1}\sin(k\chi_c)K_m(k). \quad (47)$$

We can substitute (45) into this to find

$$\int_0^\infty dk\ k^m\sin(k\chi_c)K'_m(k) = -\frac{\pi\chi_c(2m)!}{2^{m+1}m!}\left(\frac{1}{1+\chi_c^2}\right)^{m+1/2} - m\int_0^\infty dk\ k^{m-1}\sin(k\chi_c)K_m(k). \quad (48)$$

Now, we note that the derivative of the second term on the right-hand side of (48) with respect to $\chi_c$ relates to (45) via

$$\frac{\partial}{\partial\chi_c}\left(\int_0^\infty dk\ k^{m-1}\sin(k\chi_c)K_m(k)\right) = \int_0^\infty dk\ k^m\cos(k\chi_c)K_m(k) \quad (49)$$

and so

$$\int_0^\infty dk\ k^{m-1}\sin(k\chi_c)K_m(k) = \int d\chi_c\left(\frac{\pi(2m)!}{2^{m+1}m!}\left(\frac{1}{1+\chi_c^2}\right)^{m+1/2}\right). \quad (50)$$

To solve (50), we perform the substitution $\chi_c = \tan\theta_c$, and so $\cos\theta_c = 1/(1+\chi_c^2)^{1/2}$, finding

$$\int d\chi_c\left(\frac{1}{1+\chi_c^2}\right)^{m+1/2} = \int d\theta_c\ \cos^{2m-1}\theta_c. \quad (51)$$

Changing variables to $u = \sin\theta_c$, (51) can be expanded as

$$\int d\theta_c\ \cos^{2m-1}\theta_c = \int du\ \left(1-u^2\right)^{m-1} = \sum_{k=0}^{m-1}\frac{(-1)^k}{2k+1}\binom{m-1}{k}u^{2k+1} \quad (52)$$

where we have applied the binomial theorem

$$(A+B)^n = \sum_{k=0}^{n}\binom{n}{k}A^{n-k}B^k. \quad (53)$$

Therefore, (50) can be expressed as

$$\int_0^\infty dk\ k^{m-1}\sin(k\chi_c)K_m(k) = \frac{\pi(2m)!}{2^{m+1}m!}\sum_{k=0}^{m-1}\frac{(-1)^k}{2k+1}\binom{m-1}{k}\left(\frac{\chi_c^2}{1+\chi_c^2}\right)^{k+1/2}. \quad (54)$$

Then, we note that we can perform derivatives of (47) with respect to $\chi_c$ an odd or even number of times to match (43) and (44)

$$\frac{\partial^{2\nu+1}}{\partial\chi_c^{2\nu+1}}\left(\int_0^\infty dk\ k^m\sin(k\chi_c)K'_m(k)\right) = (-1)^\nu\times\int_0^\infty dk\ k^{2\nu+m+1}\cos(k\chi_c)K'_m(k) \quad (55)$$

$$\frac{\partial^{2\nu}}{\partial\chi_c^{2\nu}}\left(\int_0^\infty dk\ k^m\sin(k\chi_c)K'_m(k)\right) = (-1)^\nu\times\int_0^\infty dk\ k^{2\nu+m}\sin(k\chi_c)K'_m(k). \quad (56)$$

Thus, the symmetric and antisymmetric integral cases, (43) and (44), have the same result

$$\beta_{n+m,m}(\chi_c) = \frac{\pi(2m)!}{2^{m+1}m!}\frac{\partial^n}{\partial\chi_c^n}\left[\chi_c\left(\frac{1}{1+\chi_c^2}\right)^{m+1/2} + m\sum_{k=0}^{m-1}\frac{(-1)^k}{2k+1}\binom{m-1}{k}\left(\frac{\chi_c^2}{1+\chi_c^2}\right)^{k+1/2}\right] \quad (57)$$

where $n = 2\nu + 1$ in the symmetric case and $n = 2\nu$ in the antisymmetric case. In the case where $m = 0$, (57) simplifies to

$$\beta_{n,0}(\chi_c) = \frac{\pi}{2}\frac{\partial^n}{\partial \chi_c^n}\left(\frac{\chi_c}{\sqrt{1+\chi_c^2}}\right). \tag{58}$$

## Appendix D
## Solving the Ellipses Harmonic Weighting Function

Here, we obtain the complete class of integrals

$$\gamma^{-}_{2(\nu+\mu),2\mu}(\chi_c, \psi_c) = (-1)^{\nu+\mu} \times \int_0^\infty dk\ k^{2(\nu+\mu)} J_{2\mu}(k\psi_c)\sin(k\chi_c)K'_{2\mu}(k) \tag{59}$$

$$\gamma^{-}_{2(\nu+\mu)-1,2\mu-1}(\chi_c, \psi_c) = (-1)^{\nu+\mu} \times \int_0^\infty dk\ k^{2(\nu+\mu)-1} J_{2\mu-1}(k\psi_c)\cos(k\chi_c)K'_{2\mu-1}(k) \tag{60}$$

which we refer to as the even and odd degree antisymmetric cases, respectively, and

$$\gamma^{+}_{2(\nu+\mu)+1,2\mu}(\chi_c, \psi_c) = \frac{\partial \gamma^{-}_{2(\nu+\mu),2\mu}(\chi_c, \psi_c)}{\partial \chi_c} \tag{61}$$

$$\gamma^{+}_{2(\nu+\mu),2\mu-1}(\chi_c, \psi_c) = \frac{\partial \gamma^{-}_{2(\nu+\mu)-1,2\mu-1}(\chi_c, \psi_c)}{\partial \chi_c} \tag{62}$$

which we refer to as the even and odd degree symmetric cases, respectively, for $0 < \psi_c < \chi_c$, $\nu \in \mathbb{Z}^{0+}$, and $\mu \in \mathbb{Z}^{+}$. Here, we define

$$S_m(\chi_c, \psi_c) = i^m \tilde{S}_m(\chi_c, \psi_c) \tag{63}$$

where

$$\tilde{S}_m(\chi_c, \psi_c) = \int_0^\infty dk\ J_m(k\psi_c)\cos(k\chi_c)K_m(k). \tag{64}$$

Equation (64) has the known solution [59]

$$\tilde{S}_m(\chi_c, \psi_c) = \frac{(1-i)}{2i^m\sqrt{2\psi_c}} Q_{m-1/2}\left(i\frac{\psi_c^2 - \chi_c^2 - 1}{2\psi_c}\right) \tag{65}$$

where $Q_{m-1/2}(z)$ is a Legendre polynomial of the second kind of half-integer order, $m - 1/2$, for $m \in \mathbb{Z}^{+}$.

Now, let us integrate the right-hand side of (64) by parts

$$\int_0^\infty dk\ J_m(k\psi_c)\cos(k\chi_c)k^m K_m(k) = -\frac{\psi_c}{\chi_c}\int_0^\infty dk\ J_{m-1}(k\psi_c)\sin(k\chi_c)k^m K_m(k) - \frac{1}{\chi_c}\int_0^\infty dk\ J_m(k\psi_c)\sin(k\chi_c)k^m K'_m(k). \tag{66}$$

We shall use a standard formula for the derivative of the Bessel function of the first kind [46]

$$J_{m-1}(k\psi_c) = \frac{1}{k}\left[\frac{\partial J_m(k\psi_c)}{\partial \psi_c} + \frac{m}{\psi_c}J_m(k\psi_c)\right]. \tag{67}$$

We substitute (67) into (66) and rearrange to find

$$\int_0^\infty dk\ J_m(k\psi_c)\sin(k\chi_c)k^m K'_m(k) = \left[-\chi_c\int_0^\infty dk\ J_m(k\psi_c)\cos(k\chi_c)k^m K_m(k) - m\int_0^\infty dk\ J_m(k\psi_c)\sin(k\chi_c)k^{m-1}K_m(k) - \psi_c\frac{\partial}{\partial\psi_c}\left(\int_0^\infty dk\ J_m(k\psi_c)\sin(k\chi_c)k^{m-1}K_m(k)\right)\right]. \tag{68}$$

Now, substituting $m = 2\mu$ into (63) and (64), we can perform derivatives with respect to $\chi_c$, $2\mu$, and $(2\mu - 1)$ times, to find

$$\frac{\partial^{2\mu} S_m(\chi_c, \psi_c)}{\partial \chi_c^{2\mu}} = \int_0^\infty dk\ k^{2\mu} J_{2\mu}(k\psi_c)\cos(k\chi_c)K_{2\mu}(k) \tag{69}$$

and

$$\frac{\partial^{2\mu-1} S_m(\chi_c, \psi_c)}{\partial \chi_c^{2\mu-1}} = \int_0^\infty dk\ k^{2\mu-1} J_{2\mu}(k\psi_c)\sin(k\chi_c)K_{2\mu}(k) \tag{70}$$

respectively. Then, substituting (69) and (70) into (68), for $m = 2\mu$, we find

$$\int_0^\infty dk\ J_{2\mu}(k\psi_c)\sin(k\chi_c)k^{2\mu}K'_{2\mu}(k) = \left[-\chi_c\frac{\partial^{2\mu} S_m(\chi_c, \psi_c)}{\partial \chi_c^{2\mu}} - 2\mu\frac{\partial^{2\mu-1} S_m(\chi_c, \psi_c)}{\partial \chi_c^{2\mu-1}} - \psi_c\frac{\partial^{2\mu} S_m(\chi_c, \psi_c)}{\partial \chi_c^{2\mu-1}\partial\psi_c}\right]. \tag{71}$$

We can follow the same steps as applied to (66) with the integral:

$$\int_0^\infty dk\ J_m(k\psi_c)\sin(k\chi_c)k^m K_m(k) \tag{72}$$

for $m = 2\mu - 1$, to find

$$\int_0^\infty dk\ J_{2\mu-1}(k\psi_c)\cos(k\chi_c)k^{2\mu-1}K'_{2\mu-1}(k) = i\left[-\chi_c\frac{\partial^{2\mu-1} S_m(\chi_c, \psi_c)}{\partial \chi_c^{2\mu-1}} - (2\mu-1)\frac{\partial^{2(\mu-1)} S_m(\chi_c, \psi_c)}{\partial \chi_c^{2(\mu-1)}} - \psi_c\frac{\partial^{2\mu-1} S_m(\chi_c, \psi_c)}{\partial \chi_c^{2(\mu-1)}\partial\psi_c}\right]. \tag{73}$$

Then, we can finally generalize all cases in (71) and (73) where the degree is even or odd and perform derivatives with respect to $\chi_c$, to find

$$\gamma_{n+m,m}(\chi_c, \psi_c) = (-1)^{m+1}\frac{\partial^n}{\partial \chi_c^n}\left[\chi_c\frac{\partial^m \tilde{S}_m(\chi_c, \psi_c)}{\partial \chi_c^m} + m\frac{\partial^{m-1}\tilde{S}_m(\chi_c, \psi_c)}{\partial \chi_c^{m-1}} + \psi_c\frac{\partial^m \tilde{S}_m(\chi_c, \psi_c)}{\partial \chi_c^{m-1}\partial\psi_c}\right] \tag{74}$$

where $n = 2\nu + 1$ in the symmetric cases and $n = 2\nu$ in the antisymmetric cases.

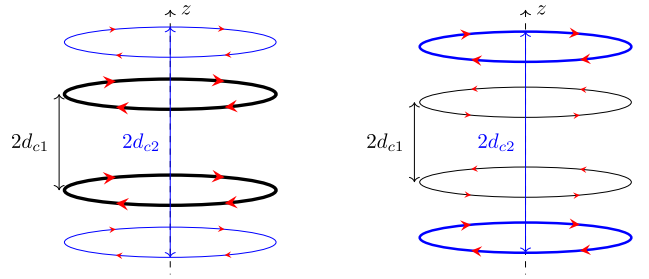


Fig. 13. Schematics of $N_{\text{loops}}$ axially symmetric loop pairs (red arrows indicate current flow direction) of radius $\rho_c$ at axial positions $z' = \pm d_{ci}$ for $i \in [1{:}N_{\text{loops}}]$. (a) $N_{\text{loops}} = 2$ pairs of loops with $d_{ci} = [0.4537, 0.9454]\rho_c$ and turn ratios 3:1 (black, blue, respectively, with higher turn ratios in bold lines) (b) $N_{\text{loops}} = 2$ pairs of loops with $d_{ci} = [0.3775, 0.9020]\rho_c$ and turn ratios $-1{:}2$, labeled as (a).

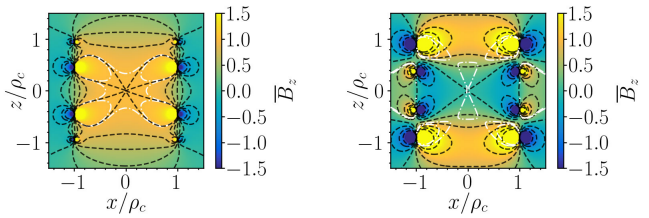


Fig. 14. Magnitude of the normalized axial magnetic field (color scales right), $\overline{B}_z = B_z/B_0$, where $B_0$ is the magnetic field strength specified in Table II, in the $xz$ plane generated by the coils in Fig. 13(a) and (b), corresponding to (a) and (b), respectively, where the coils are of radius $\rho_c$. White contours enclose the regions where (a) $B_z$ and (b) $\mathrm{d}^2B_z/dz^2$ deviate from perfect uniformity and curvature, respectively, by less than 1% and 10%, respectively (dot-dashed curves).

TABLE II

PROPERTIES OF THE OPTIMIZED COILS IN FIG. 13, HERE GIVEN FOR A COIL RADIUS OF $\rho_c = 10$ cm AND LABELED AS TABLE I. THE MAGNETIC FIELD STRENGTH, $B_0$, IS THE VALUE OF $B_z$ FOR $\mathbf{B}_{1,0}$ AND $\mathrm{d}^2B_z/dz^2$ FOR $\mathbf{B}_{3,0}$ AND IS EVALUATED AT THE CENTER OF THE COIL PER UNIT CURRENT, $I$

| $\mathbf{B}_{n,m}$ | Coil | $\max(\chi_c)$, (cm) | $l$, (m) | $B_0/I$ | $L$, ($\mu$H) |
|---|---|---|---|---|---|
| $\mathbf{B}_{1,0}$ | Fig. 13a | 9.45 | 5.03 | 33.3 $\mu$T/A | 13.8 |
| $\mathbf{B}_{3,0}$ | Fig. 13b | 9.02 | 3.77 | 3.2 mT/Am$^2$ | 4.69 |

## APPENDIX E
## SUPPLEMENTARY COIL DESIGNS

Sets of symmetric loops are presented in Fig. 13 which are optimized to generate the $\mathbf{B}_{1,0}$ and $\mathbf{B}_{3,0}$ field harmonics, displayed in (6) and

$$\mathbf{B}_{3,0}(x, y, z) = \frac{3}{4}\sqrt{\frac{7}{\pi}}\left(-2xz\hat{\mathbf{x}} - 2yz\hat{\mathbf{y}} + \left(-x^2 - y^2 + 2z^2\right)\hat{\mathbf{z}}\right). \tag{75}$$

These designs are optimized using our *Mathematica* program stored in the repository listed in [47]. The magnetic fields generated by the coils are displayed in Fig. 14 and their properties are summarized in Table II.

## ACKNOWLEDGMENT

The authors acknowledge Sionnach Devlin, a Senior Technician at the School of Physics and Astronomy Workshop, for his assistance in 3-D-printing the coil former.

## DECLARATIONS

Peter J. Hobson, Michael Packer, Matthew J. Brookes, Richard Bowtell, and Mark Fromhold have a worldwide patent (WO/2021/053356) which includes some of the coil design techniques applied in this work. Noah L. Hardwicke is a paid employee of Wolfram Research, Inc., Champaign, IL, USA, who make *Mathematica*. Niall Holmes, Matthew J. Brookes, and Richard Bowtell hold founding equity in Cerca Magnetics Ltd., Nottingham, U.K., who commercialize atomic magnetometer technology. Alister Davis, Thomas X. Smith, Chris Morley, and Max A. Weil declare no competing interests.

All supporting data may be made available on request. Our *Mathematica* Program used to generate the coil designs presented in this work is publicly available for noncommercial use [47].



## REFERENCES

[1] S. S. Hidalgo-Tobon, "Theory of gradient coil design methods for magnetic resonance imaging," *Concepts Magn. Reson. A*, vol. 36A, no. 4, pp. 223–242, Jul. 2010.

[2] Y. Wang, F. Liu, Y. Li, F. Tang, and S. Crozier, "Asymmetric gradient coil design for use in a short, open bore magnetic resonance imaging scanner," *J. Magn. Reson.*, vol. 269, pp. 203–212, Aug. 2016.

[3] X. Kong et al., "Gradient coil design method specifically for permanent-magnet-type low field portable MRI brain scanner," *IEEE Trans. Instrum. Meas.*, vol. 72, pp. 1–12, 2023.

[4] A. Pérez Galván et al., "High uniformity magnetic coil for search of neutron electric dipole moment," *Nucl. Instrum. Methods Phys. Res. A, Accel. Spectrom. Detect. Assoc. Equip.*, vol. 660, no. 1, pp. 147–153, Dec. 2011.

[5] S. Afach et al., "Dynamic stabilization of the magnetic field surrounding the neutron electric dipole moment spectrometer at the Paul Scherrer institute," *J. Appl. Phys.*, vol. 116, no. 8, Aug. 2014, Art. no. 084510.

[6] M. Rawlik et al., "A simple method of coil design," *Amer. J. Phys.*, vol. 86, no. 8, pp. 602–608, Aug. 2018.

[7] C. M. Sutton and M. T. Clarkson, "A magnet system for the MSL Watt balance," *Metrologia*, vol. 51, no. 2, pp. S101–S106, Apr. 2014.

[8] S. Li, S. Schlamminger, and Q. Wang, "A simple improvement for permanent magnet systems for Kibble balances: More flat field at almost no cost," *IEEE Trans. Instrum. Meas.*, vol. 69, no. 10, pp. 7752–7760, Oct. 2020.

[9] S. Schlamminger, L. Keck, F. Seifert, L. S. Chao, D. Haddad, and S. Li, "Calculation of magnetic forces and torques on the Kibble coil," *Metrologia*, vol. 59, no. 6, Oct. 2022, Art. no. 065002.

[10] N. Holmes et al., "A bi-planar coil system for nulling background magnetic fields in scalp mounted magnetoencephalography," *NeuroImage*, vol. 181, pp. 760–774, Nov. 2018.

[11] M. Packer et al., "Optimal inverse design of magnetic field profiles in a magnetically shielded cylinder," *Phys. Rev. Appl.*, vol. 14, no. 5, Nov. 2020, Art. no. 054004.

[12] M. Packer et al., "Planar coil optimization in a magnetically shielded cylinder," *Phys. Rev. Appl.*, vol. 15, no. 6, Jun. 2021, Art. no. 064006.

[13] K. Yang et al., "In situ compensation of triaxial magnetic field gradient for atomic magnetometers," *IEEE Trans. Instrum. Meas.*, vol. 71, pp. 1–8, 2022.

[14] J. D. Zipfel, S. Santosh, P. Bevington, and W. Chalupczak, "Object composition identification by measurement of local radio frequency magnetic fields with an atomic magnetometer," *Appl. Sci.*, vol. 12, no. 16, p. 8219, Aug. 2022.

[15] L. M. Rushton, T. Pyragius, A. Meraki, L. Elson, and K. Jensen, "Unshielded portable optically pumped magnetometer for the remote detection of conductive objects using eddy current measurements," *Rev. Sci. Instrum.*, vol. 93, no. 12, Dec. 2022, Art. no. 125103.

[16] Y.-H. Ji et al., "An actively compensated 8 nT-level magnetic shielding system for 10-m atom interferometer," *Rev. Sci. Instrum.*, vol. 92, no. 8, Aug. 2021, Art. no. 083201.

[17] P. J. Hobson et al., "Bespoke magnetic field design for a magnetically shielded cold atom interferometer," *Sci. Rep.*, vol. 12, no. 1, pp. 1–10, Jun. 2022.

[18] I. Moric et al., "Magnetic shielding of the cold atom space clock PHARAO," *Acta Astronautica*, vol. 102, pp. 287–294, Sep. 2014.

[19] A. A. Petrov et al., "Features of magnetic field stabilization in caesium atomic clock for satellite navigation system," *J. Phys., Conf. Ser.*, vol. 1038, no. 1, Jun. 2018, Art. no. 012032.

[20] T. M. Hoang et al., "Integrated physics package of micromercury trapped ion clock with $10^{-14}$-level frequency stability," *Appl. Phys. Lett.*, vol. 119, no. 4, Jul. 2021, Art. no. 044001.

[21] J. R. Goldman, T. D. Ladd, F. Yamaguchi, and Y. Yamamoto, "Magnet designs for a crystal-lattice quantum computer," *Appl. Phys. A, Solids Surf.*, vol. 71, no. 1, pp. 11–17, Jul. 2000.

[22] M. F. Brandl et al., "Cryogenic setup for trapped ion quantum computing," *Rev. Sci. Instrum.*, vol. 87, no. 11, Nov. 2016, Art. no. 113103.

[23] W. Wu, B. Zhou, G. Liu, L. Chen, J. Wang, and J. Fang, "Novel nested saddle coils used in miniature atomic sensors," *AIP Adv.*, vol. 8, no. 7, Jul. 2018, Art. no. 075126.

[24] J. Wang et al., "An improved target-field method for the design of uniform magnetic field coils in miniature atomic sensors," *IEEE Access*, vol. 7, pp. 74800–74810, 2019.

[25] H. Pang et al., "Design of highly uniform field coils based on the magnetic field coupling model and improved PSO algorithm in atomic sensors," *IEEE Trans. Instrum. Meas.*, vol. 71, pp. 1–11, 2022.

[26] M. C. D. Tayler et al., "Miniature biplanar coils for alkali-metal-vapor magnetometry," *Phys. Rev. Appl.*, vol. 18, no. 1, Jul. 2022, Art. no. 014036.

[27] R. Turner, "A target field approach to optimal coil design," *J. Phys. D, Appl. Phys.*, vol. 19, no. 8, pp. L147–L151, Aug. 1986.

[28] L. K. Forbes and S. Crozier, "A novel target-field method for finite-length magnetic resonance shim coils: I. Zonal shims," *J. Phys. D, Appl. Phys.*, vol. 34, no. 24, pp. 3447–3455, Dec. 2001.

[29] L. K. Forbes and S. Crozier, "A novel target-field method for finite-length magnetic resonance shim coils: II. Tesseral shims," *J. Phys. D, Appl. Phys.*, vol. 35, no. 9, pp. 839–849, May 2002.

[30] L. K. Forbes and S. Crozier, "A novel target-field method for magnetic resonance shim coils: III. Shielded zonal and tesseral coils," *J. Phys. D, Appl. Phys.*, vol. 36, no. 2, pp. 68–80, Jan. 2003.

[31] J. W. Carlson, K. A. Derby, K. C. Hawryszko, and M. Weideman, "Design and evaluation of shielded gradient coils," *Magn. Reson. Med.*, vol. 26, no. 2, pp. 191–206, Aug. 1992.

[32] M. Packer et al., "Magnetic field design in a cylindrical high-permeability shield: The combination of simple building blocks and a genetic algorithm," *J. Appl. Phys.*, vol. 131, no. 9, Mar. 2022, Art. no. 093902.

[33] C. B. Crawford, "The physical meaning of the magnetic scalar potential and its use in the design of hermetic electromagnetic coils," *Rev. Sci. Instrum.*, vol. 92, no. 12, Dec. 2021, Art. no. 124703.

[34] N. Nouri and B. Plaster, "Comparison of magnetic field uniformities for discretized and finite-sized standard, solenoidal, and spherical coils," *Nucl. Instrum. Methods Phys. Res. A, Accel. Spectrom. Detect. Assoc. Equip.*, vol. 723, pp. 30–35, Sep. 2013.

[35] F. Roméo and D. I. Hoult, "Magnet field profiling: Analysis and correcting coil design," *Magn. Reson. Med.*, vol. 1, no. 1, pp. 44–65, Mar. 1984.

[36] M. J. E. Golay, "Field homogenizing coils for nuclear spin resonance instrumentation," *Rev. Sci. Instrum.*, vol. 29, no. 4, pp. 313–315, Apr. 1958.

[37] F. Bonetto, E. Anoardo, and M. Polello, "Saddle coils for uniform static magnetic field generation in NMR experiments," *Concepts Magn. Reson. B, Magn. Reson. Eng.*, vol. 29B, no. 1, pp. 9–19, 2006.

[38] F. Zhao, X. Zhou, W. Zhou, X. Zhang, K. Wang, and W. Wang, "Research on the design of axial uniform coils for residual field compensation in magnetically shielded cylinder," *IEEE Trans. Instrum. Meas.*, vol. 71, pp. 1–9, 2022.

[39] Q. Cao et al., "Design of highly uniform magnetic field cylinder coils based on grey wolf optimizer algorithm in atomic sensors," *IEEE Sensors J.*, vol. 21, no. 18, pp. 19922–19929, Sep. 2021.

[40] J. Simpson et al., "Simple analytic expressions for the magnetic field of a circular current loop," NASA, Washington, DC, USA, Tech. Rep. 20010038494, 2001.

[41] G. E. Lee-Whiting, "Uniform magnetic fields," At. Energy Canada Ltd., Chalk River, ON, Canada, Tech. Rep. AECL–419, Feb. 1957. [Online]. Available: https://inis.iaea.org/search/search.aspx?orig_q=RN:53119313

[42] W. Zhou, B. Han, J. Wang, D. Wu, F. Zhao, and N. Li, "Design of uniform magnetic field coil by quasi-elliptic function fitting method with multiple optimizations in miniature atomic sensors," *IEEE Trans. Ind. Electron.*, vol. 69, no. 11, pp. 11755–11764, Nov. 2022.

[43] J. L. Kirschvink, "Uniform magnetic fields and double-wrapped coil systems: Improved techniques for the design of bioelectromagnetic experiments," *Bioelectromagnetics*, vol. 13, no. 5, pp. 401–411, 1992.

[44] P. J. Hobson et al., "Analytic models of cylindrical magnetic coil building blocks," in *Proc. Conf. Precis. Electromagn. Meas.*, 2022, pp. 1–15.

[45] E. L. Hill, "The theory of vector spherical harmonics," *Amer. J. Phys.*, vol. 22, no. 4, pp. 211–214, Apr. 1954.

[46] P. M. Morse and H. Feshbach, *Methods of Theoretical Physics*. New York, NY, USA: McGraw-Hill, 1953.

[47] N. L. Hardwicke, P. J. Hobson, and M. Packer. (2023). *NoahHardwicke/CreateCoil*. [Online]. Available: https://github.com/NoahHardwicke/CreateCoil

[48] E. M. Purcell, *Electricity and Magnetism*, 2nd ed. New York, NY, USA: McGraw-Hill, 1985.

[49] R. Turner, "Minimum inductance coils," *J. Phys. E, Sci. Instrum.*, vol. 21, no. 10, pp. 948–952, Oct. 1988.

[50] J. E. Dennis and R. B. Schnabel, *Globally Convergent Modifications of Newton's Method*. Philadelphia, PA, USA: SIAM, 1996, ch. 6, pp. 111–154.

[51] P. J. Hobson et al., "Benchtop magnetic shielding for benchmarking atomic magnetometers," 2022, *arXiv:2210.15612*.

[52] X.-T. Xu, Z.-Y. Wang, R.-H. Jiao, C.-R. Yi, W. Sun, and S. Chen, "Ultra-low noise magnetic field for quantum gases," *Rev. Sci. Instrum.*, vol. 90, no. 5, May 2019, Art. no. 054708.

[53] V. S. Chauhan, S. Bhushan, and R. K. Easwaran, "Magnetic coil design for two dimensional magneto optical trap to realization of efficient quantum memory," in *Proc. AIP Conf.*, vol. 2241, no. 1, 2020, Art. no. 020012.

[54] N. Holmes et al., "A lightweight magnetically shielded room with active shielding," *Sci. Rep.*, vol. 12, no. 1, pp. 1–8, Aug. 2022.

[55] G. M. Voss, A. Bond, J. E. G. Edwards, and T. C. Hender, "Toroidal field coil design for the spherical tokamak power plant," *Fusion Eng. Des.*, vol. 48, nos. 3–4, pp. 407–418, Sep. 2000.

[56] R. Mukesh, K. Lingadurai, and U. Selvakumar, "Airfoil shape optimization using non-traditional optimization technique and its validation," *J. King Saud Univ.-Eng. Sci.*, vol. 26, no. 2, pp. 191–197, Jul. 2014.

[57] J. Bonnans and A. Shapiro, *Perturbation Analysis of Optimization Problems*. Cham, Switzerland: Springer, Jan. 2000.

[58] J. J. C. Mulder, "Closed-form spherical harmonics: Explicit polynomial expression for the associated Legendre functions," *J. Chem. Educ.*, vol. 77, no. 2, p. 244, Feb. 2000.

[59] I. S. Gradshteyn and I. M. Ryzhik, *Table of Integrals, Series, and Products*, 7th ed. Amsterdam, The Netherlands: Elsevier, 2007.


**Peter J. Hobson** received the M.Phys. degree in theoretical physics from Durham University in 2018, the M.Res. degree in translational quantum technology from the University of Birmingham in 2020, and the Ph.D. in physics from the University of Nottingham in 2022.

He is currently an EPSRC Doctoral Prize Fellow with the University of Nottingham. His research interests include magnetic field design, optimizing electromagnetic shielding, and next-generation quantum sensors.

**Noah L. Hardwicke** is currently pursuing the B.Sc. degree in physics with the University of Nottingham.

He is currently an Employee with Wolfram Research, Inc., where he develops user interfaces for Wolfram Language products, particularly those which assist in writing code.

**Alister Davis** received the M.Phys. degree (Hons.) in physics from the University of Nottingham in 2019, where he is currently pursuing the Ph.D. degree in theoretical physics.

His research focuses on magnetic shielding for quantum experiments. He has a particular interest in enabling the easier design and manufacturing of complex coil designs.

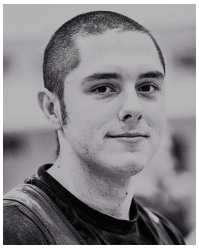

**Thomas X. Smith** received the M.Phys. degree in physics from the University of Nottingham in 2022, where he is currently pursuing the Ph.D. degree in physics, where his research focuses on the design and creation of additively manufactured magnetic shields.

**Chris Morley** received the M.Sci. degree in physics and the Ph.D. degree from the University of Nottingham in 2016 and 2020, respectively. He successfully defended his thesis "Optimization and Simulation of Magneto Optical Traps for Quantum Technologies" in 2020.

He is currently a Post-Doctoral Researcher with the University of Nottingham, where his work focuses on magnetic field design and simulations to enable emerging quantum technologies.

**Michael Packer** received the M.Sci. degree in theoretical physics from the University of Birmingham in 2016 and the Ph.D. degree in physics from the University of Nottingham in 2021.

Then, he went on to be a Post-Doctoral Researcher at the University of Nottingham, where his research focused on the optimization of interacting electromagnetic systems, before transitioning into quantitative financial research.

**Niall Holmes** received the M.Sci. and Ph.D. degrees in physics from the University of Nottingham in 2016 and 2020, respectively.

He is currently a Research Fellow with the Sir Peter Mansfield Imaging Centre, University of Nottingham, developing active magnetic field control for biomagnetic measurements, particularly wearable magnetoencephalography.

**Max A. Weil** received the M.Sci. degree (Hons.) in physics from the University of Nottingham in 2022.

His research interests include magnetic field design, solar interactions with the terrestrial geomagnetic field, and the development of magnetic traps for laser-cooled atoms.

**Matthew J. Brookes** received the Ph.D. degree from the University of Nottingham in 2005.

He is currently a Professor of physics with the University of Nottingham. His research interests include the development and application of multimodal functional brain imaging and the brain imaging modality called magnetoencephalography. These techniques are having a significant impact on multiple clinical fields, including examining traumatic head injuries and diagnosing schizophrenia and epilepsy.

**Richard Bowtell** received the B.A. degree in natural sciences from Cambridge University in 1984 and the Ph.D. degree in physics from the University of Nottingham in 1988.

He has spent his career at the School of Physics and Astronomy, Nottingham, where he was appointed as a Lecturer in 1989 and the Chair in 2000. He has served as the Head of the School of Physics and Astronomy from 2008 to 2014 and currently the Director of the Sir Peter Mansfield Imaging Centre. His research interests span magnetic resonance imaging and spectroscopy and magnetoencephalography and include the design of magnetic field control systems for both modalities.

**Mark Fromhold** received the B.Sc. degree (Hons.) in physics from Durham University in 1986 and the Ph.D. degree in the theory of quantum tunneling in semiconductor heterostructures from the University of Nottingham in 1990.

After post-doctoral research at the University of Warwick and an EPSRC U.K. Advanced Research Fellowship, in 2000, he rejoined the University of Nottingham and has been the Head of the School of Physics and Astronomy since August 2020. His current research interests include the development and integration of electronic, cold-atom, and electromagnetic systems as components for quantum technologies.